Continental Shelf Research 31 (2011) 1541–1557

Contents lists available at ScienceDirect

Continental Shelf Research

journal homepage: www.elsevier.com/locate/csr

Reviews

Simulation of irregular waves in an offshore wind farm with a spectral wave model

S. Ponce de León [a,*], J.H. Bettencourt [b], N. Kjerstad [a]

[a] Ålesund University College, Department of Technology and Nautical Sciences, Larsgårdsvegen 2, 6009 Ålesund, Norway
[b] Institute for Cross-Disciplinary Physics and Complex Systems (IFISC), Spanish National Research Council (CSIC), University of Balearic Islands (UiB), Edifici Instituts Universitaris de Recerca, Campus Universitat de les Illes Balears, E-07122, Palma de Mallorca, Spain

ARTICLE INFO

Article history:
Received 15 December 2010
Received in revised form
4 July 2011
Accepted 13 July 2011
Available online 22 July 2011

Keywords:
Irregular waves
Windmill monopile
Offshore wind farm
SWAN
Norwegian continental shelf
Wave diffraction

ABSTRACT

A numerical study of irregular waves in the Norwegian continental shelf wind farm (HAVSUL-II) was conducted using 3rd generation spectral wave models. The study was composed of two parts: the study of the effect of a single windmill monopile in the local incoming wave field using an empirical JONSWAP spectrum, and a wave hindcast study in the wind farm area using realistic incoming wave spectra obtained from large scale simulations for the 1991–1992 winter period. In the single windmill monopile study the SWAN wave model was used, while the hindcast study was conducted by successively nesting from a coarse grid using the WAM model up to a high-resolution (56 m) grid covering 26.2 km^2 of the HAVSUL-II windmill farm using the SWAN model. The effect of a single monopile on incident waves with realistic spectra was also studied. In the single windmill study the monopile was represented as a closed circular obstacle and in the hindcast study it was represented as a dry grid point. The results showed that the single windmill monopile creates a shadow zone in the down wave region with lower significant wave height (H_s) values and a slight increase of H_s in the up wave region. The effects of the windmill monopile on the wave field were found to be dependent on the directional distribution of the incoming wave spectrum and also on the wave diffraction and reflection. The hindcast study showed that the group of windmill monopiles may contribute to the reduction of the wave energy inside the offshore wind farm and that once the waves enter into the offshore wind farm they experience modifications due to the presence of the windmill monopiles, which cause a blocking of the wave energy propagation resulting in an altered distribution of the H_s field.

Contents

* Corresponding author. Present address: Marine Technologies, Operational Oceanography and Sustainability Department (TMOOS), Mediterranean Institute for Advanced Studies (IMEDEA), Spanish National Research Council (CSIC), University of Balearic Islands (UiB), Escoles Velles. C/Miquel Marqués 21, 07190, Esporles, Illes Balears, Spain. Tel.: +34 659027032; fax: +34 971 61 17 61.
E-mail address: sponce@imedea.uib-csic.es (S. Ponce de León).

0278-4343/$ - see front matter © 2011 Elsevier Ltd. All rights reserved.
doi:10.1016/j.csr.2011.07.003

1. Introduction

The increasing need of energy supply is resulting in a rapid development of renewable energy sources. Offshore wind farms are one important type of renewable energy production sites, installed on coastal waters and comprising hundreds of wind turbines installed on the sea floor and supported by monopiles. The presence of these structures in coastal regions will affect coastal processes such as sediment transport and deposition regimes, tidal conditions and wave climate. These potential effects of the wind farm can occur locally, on the development site, and remotely on the far field or the coastline itself.

In the wind farm development site, the wave climate can be altered by the existence of the wind turbines support structures (monopiles) and additional wave transformation processes will be present. The assessment of these changes to the wave climate is an important task when studying the global environmental impact of offshore wind farms.

When waves approach coastlines, they can experience transformations due to refraction, shoaling and diffraction due to the changes in depth and the presence of currents. Additionally, wave energy loss can occur due to bottom friction and depth induced wave breaking. The presence of a surface piercing obstacle, such as a windmill monopile, will lead to wave diffraction around the obstacle and wave reflection from the obstacle and energy will be lost due to drag and inertia effects. The magnitude of these effects depends on the length scales of the wave and obstacle. For a cylindrical monopile, the length scale is the diameter D and the relevant parameters for the wave are the wavelength L and amplitude a. For small D/L and large a/D flow separation and vortex shedding are important but diffraction effects are negligible while for large D/L and small a/D diffraction becomes important and flow separation is insignificant (Mei, 1992).

The problem of wave interaction with a vertical cylinder has been subject to intense study for some time with focus on offshore engineering applications, mainly the calculation of the wave loads acting on the cylinder. For large D/L, under the assumption of linear theory, the problem was first solved by Havelock (1940) for deep water and by MacCamy and Fuchs (1954) for arbitrary water depth.

Kriebel (1990) proposed a closed form solution for the second order velocity potential resulting from the interaction of Stokes wave with a large circular cylinder. The related problem of wave interaction with an array of vertical cylinders was solved exactly by Linton and Evans (1990) for a linear wave.

Later, Maniar and Newman (1997), looking at an array of bottom-mounted cylinders under the assumptions of linear theory, found that when the number of cylinders is large but finite, near-resonant modes occur between adjacent cylinders caused by the existence of trapped waves in a channel.

Walker and Eatock Taylor (2005), under the assumption of linear theory, studied the diffraction of regular waves by linear arrays of vertical bottom-mounted circular cylinders using an analytical solution to the diffraction problem. They concluded that for incident regular waves at critical wave numbers, the large magnifications in force and free surface elevation that resulted could have serious implications for very large column-supported floating structures. The body of literature dedicated to this problem is wide and the reader is referred to Eatock Taylor (2007) for a review.

The basic assumption of the cited studies is a progressive monochromatic wave. However, the real sea state is composed of waves with different frequencies, propagating in distinct directions. It can then be expected that the interaction problem under realistic conditions will have different properties than those obtained from the regular wave assumption. As an example, Zhu (1993) considered the diffraction of short-crested waves by a vertical circular cylinder finding that the pressure distribution and water run-up on the cylinder was different from those of plane incident waves and that the total force exerted on the cylinder in the direction of wave propagation is smaller when compared to that induced by plane waves.

The irregular nature of the real sea state is best described by the wave energy spectrum which represents the distribution of wave energy in the range of frequencies and propagation directions. For the problem of wave loading on the cylinder in irregular seas – which is the problem of interest for most engineering applications – regular wave theory is satisfactory because its results can be combined with the spectral representation of the sea state to obtain a wave force spectrum (Dean and Dalrymple, 1991).

For the problem of wave transformation inside a wind farm, however, besides the local effects of the windmill monopile on the incident waves, there is also interest in its further propagation and transformation inside the whole development site and account must be made of the different wave generation, transformation and dissipation processes that might occur.

Traditionally the diffraction of waves is computed with phase-resolving models like the mild-slope models. But, these models do not account generally for the generation, dissipation and wave–wave interactions of the waves. Phase-averaged wave models, which describe the evolution of the wave energy spectrum as a function of time and space by solving a single advective transport equation, have become a useful tool in the last decades. The WAM (Günther et al., 1992) and SWAN (Ris, 1997; Booij et al., 1999) are the most popular of these spectral wave models because they solve the wave energy transport equation explicitly without any assumption regarding the energy spectrum shape. The SWAN model accounts for diffraction process partially using a phase-decoupled refraction–diffraction approach described in Holthuijsen et al. (2003). The approximation is based on the mild-slope equation expressed in terms of the turning rate of individual wave components in the two-dimensional wave spectrum. This approximation omits phase information, so it does not permit coherent wave fields in the computational domain (Holthuijsen et al., 2003).

A generic research on the effect of offshore wind farm was also produced for ETSU-Energy Technology Support Unit (Cooper and

Beiboer, 2002) as part of the New Renewable Energy Programme by applying MIKE21 BW model (Boussinesq equations) for an evaluation of the effects of an offshore wind farm on coastal processes in relation to a representative set of tide, wave and sediment transport conditions. From this research it was concluded that the windmill farm causes changes in current, wave and sediment conditions, although the effects are unlikely to be significant in the far field, with only small influences determined in the near-field.

Ilic et al. (2007) studied the accuracy of the diffraction model implemented in SWAN by means of field and laboratory data. Their results showed that the inclusion of diffraction in the SWAN model improved the estimation of the significant wave height (H_s) in the shadow area behind a breakwater. They also determined the optimum grid size with lowest error for achieving a stable solution and concluded that in the case of swell waves in coastal waters, the SWAN diffraction model is less accurate.

Alari and Raudsepp (in press) applied the SWAN model to an offshore wind farm representing the wind monopiles as dry grid points and showed that the reduction of significant wave height in the Baltic Sea (a semi-enclosed sea) due to a wind farm is very small. They argued that this is due to a very small ratio between the monopile diameter and dominant wavelength and the favorable setup of the monopiles with respect to each other and the coast. Their results are in accordance with the size of the basin used in the study, where the most usual wave climate is wind sea and not oceanic swell.

Beels et al. (2010) studied the wave climate in a farm of wave energy converters (WEC) and the wave height reduction behind a single WEC. Their study shows that an increase of the directional spread leads to a wave redistribution behind the WEC and that the dimensions of the wake depend on the incident wave climate. They also discussed the applicability of wave propagation models for farm modeling by analyzing the main limitations of the spectral wave model SWAN and favoring the application of the time domain models to overcome these limitations by developing their own technique using a mild-slope equation model to simulate the absorbing effect of the WEC.

From all types of existent wave models and studies on the subject of offshore wind farms it can be concluded that there does not exist a perfect model for modeling a real incoming sea state in the environment of an offshore wind farm. If the spectral models account for the generation, dissipation and wave–wave interactions of the waves some other processes such as diffraction are not accurate enough depending on the spatial resolution and the shape of the obstacles. For another hand, phase-resolving time domain (mild-slope equation and Boussinesq equation models), which represent accurately the propagation processes require a prohibitively high spatial resolutions and computational cpu time and also do not account fully for the generation and dissipation physical processes that spectral models do.

The aim of this paper is to study the transformation of irregular waves inside an offshore windmill farm using a spectral wave model. Attention was paid to local effects in the vicinity of a windmill monopile with typical diameter and to the whole wind farm.

Two different studies have been carried out in this work: the study of the effect of a single windmill monopile on incoming irregular waves using the SWAN 40.72 model in stationary mode and a hindcast study of the wave field with and without the windmills inside the offshore wind farm (HAVSUL-II) in the Norwegian continental shelf applying two 3rd generation spectral wave models: WAM 4.52 and SWAN for the winter of 1991–1992. The effect of a single windmill monopile on incident waves with realistic spectra from the hindcast was also performed using the SWAN model.

The SWAN model was chosen because it has an adequate representation of the physical phenomena in shallow and intermediate waters. In order to have realistic incoming wave energy in the HAVSUL-II wind farm the WAM model was applied to the whole North Atlantic to ensure the boundary conditions for the SWAN high resolution simulations.

This paper is structured as follows. Section 2 reviews the area of study: the HAVSUL-II wind farm located in the Norwegian continental shelf. The physics of the spectral wave models is briefly described in Section 3. Stationary simulations for a single monopile are given in Section 4. Section 5 describes the hindcast study of the whole HAVSUL-II wind farm. Section 6 deals with the nonstationary simulations for one monopile using realistic wave spectra obtained in the hindcast study and the concluding remarks are given in Section 7.

2. The HAVSUL-II study area

The Norwegian continental shelf is exposed to long period swell from the North Atlantic. The swell is mainly generated by the intense frequent extratropical cyclones that originate in the western North Atlantic east of Newfoundland, and move rapidly northeasterly across the North Atlantic (Gjevik et al., 1988) leading to narrowly peaked swell spectra with considerable energy at periods of about 15–20 s in the Norwegian region.

The Halten bank area, to the west of Norway, is characterized by high waves that occur mostly in connection with winds from the west or southwest. These winds are caused by a stable high pressure over the British Isles and the North Sea and the propagation of lows from the North Atlantic towards Halten bank (Reistad et al., 2005).

Along the Norwegian coast there are already several offshore wind farm projects in development. The HAVSUL projects consist of three offshore wind farms (HAVSUL-I, II and IV) situated off the coast of Møre and Romsdal county in Mid-Norway (Fig. 1). The coastline of Møre and Romsdal has stable and strong wind conditions, which is the single most important factor for the choice of location of a wind farm. Additionally water depth is important in the design of offshore wind farms. Due to current technological and economical constraints, the installation process requires water depths to be between 4 and 30 m, and the HAVSUL projects are located within this depth range (Kjerstad, 2006). The turbines to be installed have a height of 95 m above the sea bed and a supporting monopile with a cylindrical shape and a diameter of 6 m installed in the sea floor and are separated 540 m from each other.

3. Formulation of spectral wave models

WAM and SWAN are phase-averaged or spectral wave models that describe the evolution in time and space of the energy density wave spectrum $F(\sigma, \theta)$ as a function of the relative angular frequency $\sigma(=2\pi f)$ and wave propagation direction θ. A general form of the energy balance equation in Cartesian coordinates can be expressed as

$$\frac{\partial F}{\partial t}+\frac{\partial}{\partial x}(c_x F)+\frac{\partial}{\partial y}(c_y F)+\frac{\partial}{\partial \theta}(c_\theta F)+\frac{\partial}{\partial \sigma}(c_\sigma F)=S_{tot} \quad (1)$$

where $c_{x,y,\sigma,\theta}$ are the wave propagation components in the (x, y, σ, θ) spaces and S_{tot} the forcing term.

Equations such as (1) are classed as energy transport equations and their solution requires the specification of appropriate initial and boundary conditions, an appropriate propagation scheme to represent the transport of energy within the computational

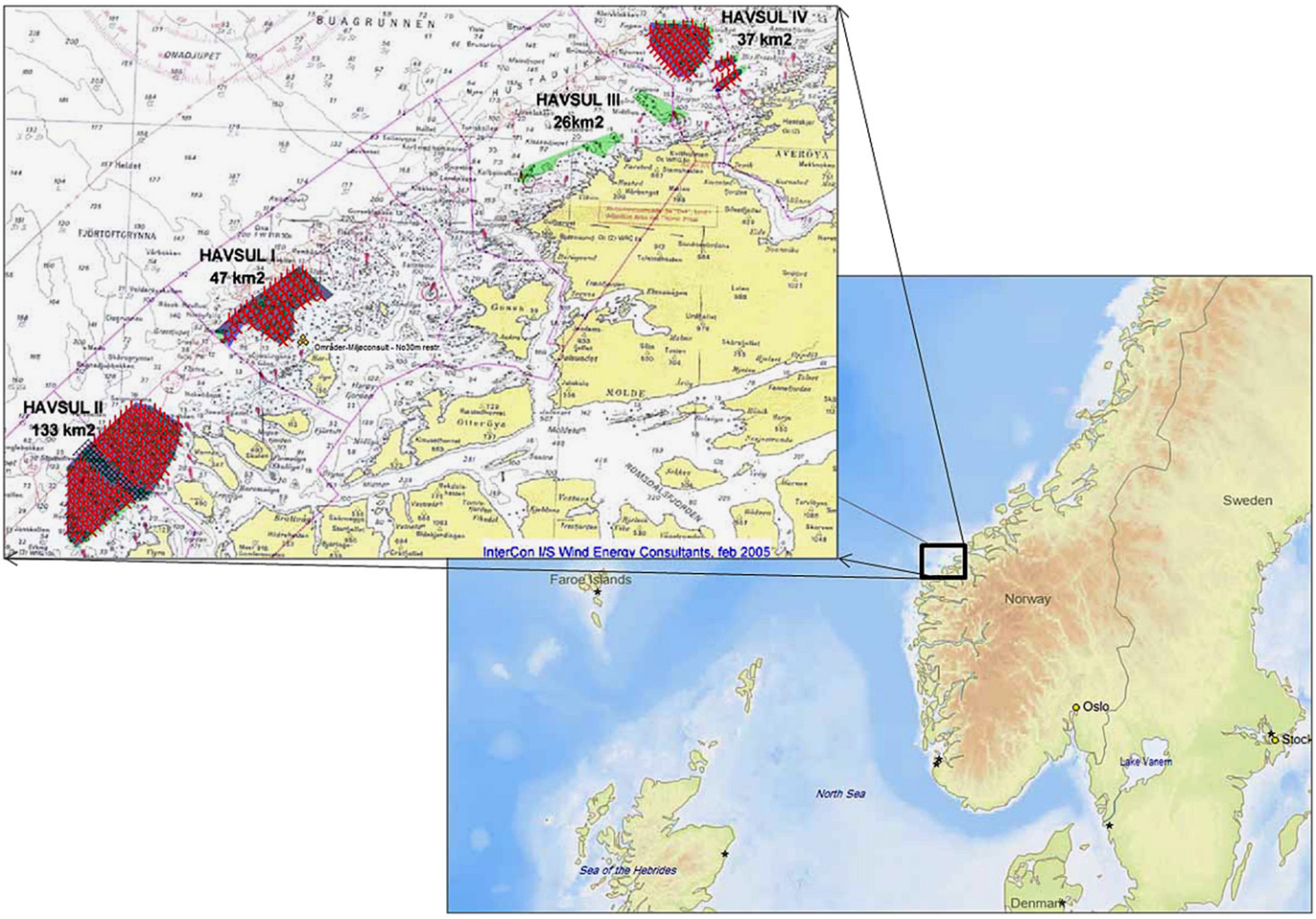

Fig. 1. Location of the offshore wind farm HAVSUL-II in the Norwegian continental shelf off the coast of Møre and Romsdal county in Norway.

Table 1
Physical processes activated in the hindcast study for the different performed simulations: without windmills, with 30 and 90 windmills (diffraction was not set for the SWAN nested grid 1).

Physical processes	WAM 4.52 (coarse grid and nested grid 1)	SWAN 40.72 (nested grid 1 and HAVSUL-II nested grid 2)
Wind input (S_{in})	Janssen (1989, 1991)	Komen et al. (1984)
Whitecapping dissipation (S_{wcap})	Komen et al. (1984)	Komen et al. (1984)
Nonlinear interactions (S_{nl4} quadruplets)	Hasselmann et al. (1985)	Hasselmann et al. (1985)
Nonlinear interactions (S_{nl3} triads)	–	Eldeberky (1996)
Bottom friction dissipation ($S_{ds,b}$)	JONSWAP	JONSWAP
Diffraction	–	Holthuijsen et al. (2003)

domain and the specification of the forcing term or source functions (Young, 1999).

In general, S_{tot} is represented as the summation of a number of the physical processes that can be modeled numerically, describing the development and the dissipation of the modeled waves in time and space

$$S_{tot} = S_{in} + S_{nl} + S_{ds} \quad (2)$$

where S_{in} represents the wind input, S_{nl} the nonlinear wave–wave interactions and S_{ds} the wave energy dissipation: whitecapping for deep water and bottom friction S_{bf} plus wave breaking S_{br} for shallow waters.

In this study we adopt the wind speed at 10 m, according to the actual version of the WAM model based on the quasi-linear model for the sea surface boundary layer from Janssen (1989, 1991).

The physical processes activated in the hindcast SWAN simulations are wave generation by wind; nonlinear interactions between three and four spectral wave components; whitecapping wave energy dissipation; bottom friction dissipation based on the empirical JONSWAP model with a constant friction coefficient equal to 0.067 $m^2\,s^{-3}$. Depth induced-breaking dissipation was switched off for this study. Diffraction was set for SWAN simulations. More details about the active physical processes are summarized in Table 1.

Although the WAM and SWAN models are both 3rd generation wave models – they solve the wave action density transport Eq. (1) without a priori spectral constraints – there are some important differences between them. WAM is a state of the art model with some shortcomings in shallow water (triad interactions which are important in nearshore areas are not considered in WAM, for example) and is more adequate for deep water and large scale

regions, whereas the SWAN model is better suited to perform high-resolution applications in shallow waters, demanding a lower computational effort than WAM due to the different propagation numerical schemes implemented. More details about the characteristics of these models can be found in Günther et al. (1992) and Booij et al. (1999).

3.1. Representation of diffraction in the SWAN model

The SWAN model represents diffraction by the phase-decoupled diffraction approach of Holthuijsen et al. (2003). It is expressed in terms of the directional turning rate of the individual wave components in the two-dimensional wave spectrum. The approximation is based on the mild-slope equation (Berkhoff, 1972) omitting phase information.

The propagation velocities in geographical and spectral spaces without diffraction denoted as $c_{x,0}$,$c_{y,0}$,$c_{\theta,0}$ are given by

$$c_{x,0} = \frac{\partial\omega}{\partial k}\cos\theta$$

$$c_{y,0} = \frac{\partial\omega}{\partial k}\sin\theta$$

$$c_{\theta,0} = -\frac{1}{k}\frac{\partial\omega}{\partial h}\frac{\partial h}{\partial n}$$

where ω is the absolute radian frequency, θ the wave direction, k the wave number and n the perpendicular to the wave ray.

The diffraction parameter δ is given by

$$\delta = \frac{\nabla(cc_g\nabla\sqrt{E})}{cc_g\sqrt{E}} \tag{3}$$

where $E(x,y)$ is the total energy of the wave field (approx. H_s^2), c the phase velocity ($c=\sigma/k$) and c_g the group velocity($c_g=\partial\sigma/\partial k$).

Due to diffraction the new propagation velocities will be

$$c_x = c_{x,o}\overline{\delta}, c_y = c_{y,o}\overline{\delta}, c_\theta = c_{\theta,0}\overline{\delta} - \frac{\partial\overline{\delta}}{\partial x}c_{y,0} - \frac{\partial\overline{\delta}}{\partial y}c_{x,0} \tag{4}$$

where $\overline{\delta} = \sqrt{1+\delta}$.

Holthuijsen et al. (2003) noted in their early studies that the wave fields showed often slight "wiggles" in geographical space that affected the calculation of gradients needed for the computation of the diffraction parameter. To remedy this, a smoothing procedure was introduced by way of a convolution filter to be applied on the wave field $E(x,y)$. This smoothing procedure is only applied to the computation of δ.

4. The single monopile

The aim of this study was to calculate the effect of a single monopile in the incoming irregular waves in simple wave propagation simulations – $S_{tot}=0$ in Eq. (1) – with constant depth and no currents. Two cases of irregular wave propagation were considered: a unidirectional irregular wave and multidirectional irregular wave. For both cases, a JONSWAP spectrum was used as incoming boundary condition. Simulations were run with and without the phase-decoupled diffraction approach implemented in SWAN to assess its effects on the results.

4.1. Representation of the monopile in the computational spatial grid

In order to represent the monopile in the computational domain, it was modeled as a circular obstacle with a diameter $D=7$ m and with its circumference divided into 16 line segments. The diameter was increased from 6 m to obtain a better representation of its shape.

In order to later understand the results it is essential to explain the treatment of obstacles in SWAN. Firstly, the obstacle feature of SWAN is mostly intended to model sub-grid, straight line obstacles in the wave field, such as breakwaters, dams, etc. In this view, the obstacle is defined by the crossing of the obstacle line with the computational grid lines, i.e., the lines joining adjacent grid points. Since the obstacle line is a sub-grid feature, no actual calculations are performed on the locations defined by the intersections of obstacle and grid lines. Instead, the propagation of wave energy between two grid points lying on opposite sides of the obstacle line is modified to take into account the presence of the obstacle. These modifications depend on the properties of the obstacle defined by the user, particularly the amount of reflection and transmission of wave energy from and through the line defining the obstacle. This is shown in Fig. 2, where four grid points (A, B, C and D) and an obstacle line are represented. The obstacle line is a chord of the circular monopile. Energy propagating from D to A will be reflected back to D by an amount specified by the reflection coefficient (R_c) of the obstacle line and an amount of energy will be transmitted from D to A, depending on the transmission coefficient (T_c) defined. The same is true for energy propagating from B to A. If the transmission coefficient is set to zero, grid point A will not receive any energy from D and B. This means that if point A is completely enclosed by the lines defining the circular obstacle and the transmission coefficients of these lines are set to zero, it will be excluded from the wave energy propagation process. Note that this does not mean that A becomes a dry point. In fact, reflection of wave energy from the obstacle at point D will only work if A is a wet point. If other grid points are also inside the circular obstacle, then these points will exchange energy during the propagation process, but not with the grid points outside of the obstacle.

In the case of grid point C, since the obstacle does not intersect the grid lines CD and BC, it will not feel the direct influence of the monopile; although an indirect influence will be felt since it will exchange energy with points B and D.

This treatment of obstacles in the wave field also means that the degree of representation of the obstacle does not depend solely on the number of segments that are used to discretized it, rather it will depend on the resolution of the computational grid, since it is the resolution that determines the amount of

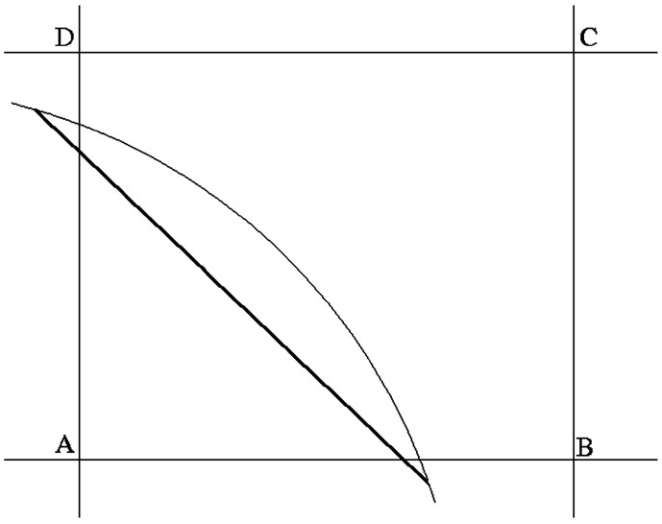

Fig. 2. Obstacle definition. A, B, C and D: computational grid points; Thick line: obstacle segment; Curve: Monopile surface.

intersections of the grid lines with the obstacle lines. Furthermore, SWAN will not compute the solution to the wave propagation equations at the actual monopile surface (curved line in Fig. 2), nor on the obstacle segment.

4.2. Setup of simulations

The computational domain was setup with 100 m of length in both X and Y directions and the spatial resolution in both directions were set at 1 m. The water depth was set at 15 m. The spectral domain was discretized in 40 frequency bins from 0.04 to 0.4 Hz, while in θ-space a full circle was used with a resolution ($\Delta\theta$) that varied from unidirectional to multidirectional simulations. Details of the simulation parameters are shown in Table 2 for the different SWAN runs performed. The directional resolution was chosen in function of the directional spreading of wave energy spectrum. Although for the M11, M12 and M21, M22 runs, the θ-space might be poorly discretized, we have run the simulations with higher resolutions and found little difference in the results.

The reflection coefficient was set to one to get an upper limit on the reflected wave energy from the monopile. The reflection type used is specular reflection where the reflected wave energy has the opposite direction of the incoming energy. The transmission coefficient was set to zero since, in realistic terms, no wave energy should penetrate the impermeable obstacle.

In the simulations with diffraction, the number of smoothing iterations was set at $n_s=28$. This value was chosen based on convergence criteria. Lower values of n_s gave poor results, especially in the case of narrow directional distributions. Ilic et al. (2007) also noted that narrow directional spectra required more smoothing iterations.

4.2.1. Numerical aspects

The simulations were performed in stationary mode with the SORDUP scheme (the default in SWAN for stationary simulations). The SORDUP is a second order upwind scheme were the action density values at a grid node are computed from the two grid nodes upstream with respect to the wave propagation direction. With respect to first order schemes, the increase in computational cost of the SORDUP scheme is not significant, but the scheme is known to produce "wiggles" in the solution (Rogers et al., 2002). Note that for grid points in the vicinity of the obstacle, SWAN reverts to a first order scheme. For propagation in spectral space SWAN uses a hybrid central/upwind scheme.

Table 2
Setup of single monopile SWAN simulations (H_s—Significant Wave Height; T_p—Peak Period; σ_θ—Standard deviation of directional distribution of wave energy spectrum; $\Delta\theta$—Directional resolution in θ-space; R_c—Reflection coefficient; T_c—Transmission coefficient; n_s—Number of smoothing steps in the calculation of diffraction parameter; (–) Diffraction not active).

Simulations	H_s (m)	T_p (s)	σ_θ (deg.)	$\Delta\theta$ (deg.)	R_c	T_c	n_s
Unidirectional							
U1	1	5	1.25	0.5	1.0	0	28
U2	1	5	1.25	0.5	1.0	0	(–)
U3	1	5	1.25	0.5	0	0	(–)
Multidirectional							
M11	1	5	10	5	0	0	28
M12	1	5	10	5	1.0	0	28
M21	1	5	10	5	0	0	(–)
M22	1	5	10	5	1.0	0	(–)
M31	1	5	30	5	0	0	28
M32	1	5	30	5	1.0	0	28
M41	1	5	30	5	0	0	(–)
M42	1	5	30	5	1.0	0	(–)

In these propagation simulations and without diffraction the absence of the depth variations and currents reduce the wave energy balance equation to its spatial propagation form

$$\frac{\partial F}{\partial t}+\frac{\partial}{\partial x}(c_x F)+\frac{\partial}{\partial y}(c_y F)=0 \tag{5}$$

When diffraction is active the wave energy balance equation (5) is augmented with the additional term of propagation in θ space and the spatial propagation velocities are modified according to Eq. (4). For a spatial grid point, the linear system of equations in (σ,θ) space becomes tridiagonal and SWAN uses the TDMA algorithm to solve it (SWAN Group, 2010).

4.3. Results

4.3.1. Unidirectional irregular waves

The purpose of these unidirectional simulations was to compare the results with analytical calculations based on the MacCamy–Fuchs theory for linear diffraction of waves by a circular cylinder. Although the linear theory was derived for monochromatic waves, using the superposition principle, the analytical results can be extended to unidirectional irregular waves as shown by Rao and Raman (1988), who used this approach to simulate wave elevations on large circular cylinders due to irregular unidirectional waves generated by wind.

For a wave energy spectral density $F(\sigma)$ discretized in S frequency components, the total free surface elevation N is given by

$$N=\sum_{n=1}^{S}\frac{H_n}{2}\eta_n=\sum_{n=1}^{S}\frac{H_n}{2}\sum_{m=0}^{\infty}\beta_m\left[J_m(k_n r)-\frac{J'_m(k_n a)}{H'_m(k_n a)}H_m(k_n r)\right]\cos m\theta e^{-i(\sigma_n t-\phi_n)} \tag{6}$$

where η_n is the nondimensional free surface elevation, J_m and H_m are the Bessel functions of the first and third kind (Hankel functions), respectively, β_m a complex constant equal to $(2-\delta_{m0})i^m$ and the primes denote derivative with respect to the function's argument. The cylinder radius is a and (r,θ) are the polar coordinates of a point with respect to the cylinder axis. The term inside the first sum in Eq. (6) is the free surface elevation of a monochromatic wave with wavenumber k_n and circular frequency σ_n, related through the dispersion relationship

$$(\sigma_n)^2=gk_n\tanh k_n h \tag{7}$$

and φ_n is a random phase lag, uniformly distributed between 0 and 2π. In Eq. (7), h is the water depth and g the gravitational acceleration. The wave height of the nth harmonic component is $H_n=2\sqrt{\sigma_n F(\sigma_n)}$.

To generate the irregular waves, a JONSWAP spectrum was used with significant wave height $H_s=1$ m, peak period $T_p=5$ s and $n=40$. The range of wave periods is from 1 to 25 s, typical of wind generated water waves (Mei, 1992).

The free surface elevation N was calculated for 78 s with a 1 s time step. From the time record of free surface elevation at each spatial point $N(x,y,t)$ the spectral density $F(\sigma,x,y)$ was obtained by Fourier analysis and the H_s was recovered by $H_s=4\sqrt{m_0}$,where m_0 is the first spectral moment of F.

The SWAN model was developed for multidirectional random seas, so a purely unidirectional random wave had to be approximated in the SWAN simulations by a multidirectional incoming wave spectrum with very low directional spreading of wave energy (Table 2).

In Fig. 3, the H_s along a circumference 1.5 m away from the cylinder surface is plotted for the analytical results and for SWAN results. The analytical curve shows a high H_s zone at the up wave area of the monopile that decreases as we move towards the down wave side, with a slight recovery at the down wave position. The high H_s at the up wave area of the cylinder is caused

by a standing wave pattern, known from the linear diffraction of a monochromatic wave by a circular cylinder (Kriebel, 1990). The SWAN results, however, show a much smaller H_s along the circumference, that in the down wave area behind the monopile decreases rapidly to zero at the down wave position.

The difference between these results is due to two limitations in the modeling of the problem. With respect to the standing wave pattern, phase-averaged wave models cannot deal with such coherent wave patterns since they lack phase information so that the high H_s area is missing from the SWAN results. With respect to the down wave area of the monopile, the reason for the low values of H_s is that the numerical scheme – an upwind scheme – will use the wave energy from the upwind grid point that in this model is inside the monopile and, since the transmission coefficient is zero, will not contribute to the energy computation in the down wave region close to cylinder. This is aggravated by the fact that wave energy is propagating in a thin directional band mainly parallel to the shadow area behind the monopile, meaning that little or no wave energy will propagate from the outside of the shadow area to behind the monopile.

When reflection is used, the H_s level in front of the monopile increases slightly, but is still below the H_s for the analytical results. The effect of diffraction can be seen on the up wave area of the monopile were the H_s distribution is slightly smoother, and also on the down wave area of the monopile where the decrease in H_s towards the down wave position has a somewhat lower slope. This is due to the smoothing effect of the diffraction process that will work to transport wave energy across wave height gradients.

Another important aspect is the coarse representation of the cylinder. With a grid resolution of 1 m the grid points outside of the cylinder will be too few to accurately represent its circular shape, which will cause "bumps" in the H_s distribution when reflection is used, especially in a narrow directional distribution case.

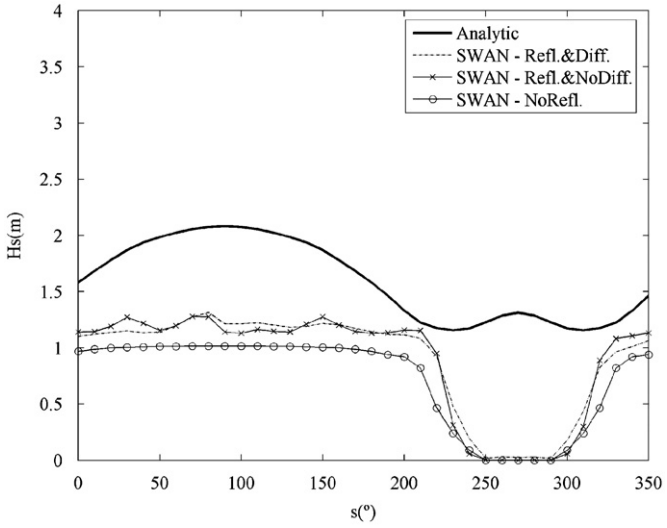

Fig. 3. H_s (m) for unidirectional irregular waves. H_s values taken along a circumference concentric with the cylindrical monopile at 5 m from its center. Up wave position ($s=90°$); Down wave position ($s=270°$). Wave propagates from the up wave to the down wave position. (Refl&Diff-U1; Refl&NoDiff-U2; NoRefl-U3).

4.3.2. *Multidirectional irregular waves*

The SWAN results for multidirectional irregular waves are shown in Figs. 4–6. The H_s along the circumference of Fig. 3 is shown in Fig. 4 for the narrow and broad directional spreading cases. The effect of reflection is clearly seen to be the increase of H_s in the up wave zone of the monopile, as in the unidirectional case. The narrow directional distribution case shows the same bumps in the H_s as in the unidirectional case, but the broad directional spreading results show a much smoother distribution of H_s. The coarse representation of the cylindrical monopile may be the reason, for that only with a broad directional spreading a smooth distribution of H_s is achieved when using reflection. The effect of diffraction is the same as in the unidirectional case, but the smoothing is nearly absent in the multidirectional case since the H_s distribution is already smooth. When reflection is turned off the H_s decreases in the up wave area, as expected. The higher directional spreading will cause a smoother transition of the H_s from the up wave to the down wave region, as the

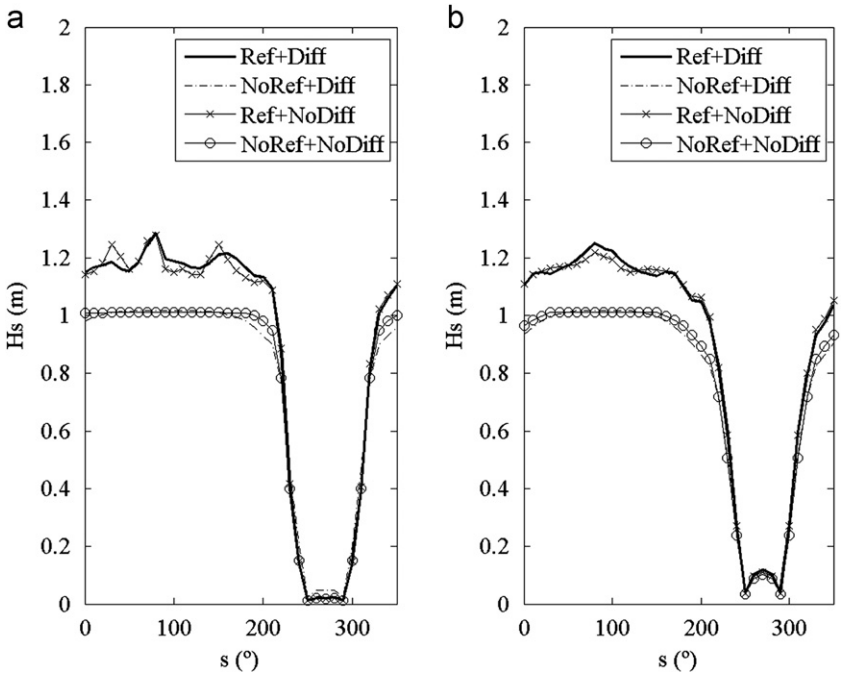

Fig. 4. H_s (m) for multidirectional irregular waves. (a) Narrow directional spreading $\sigma_\theta=10°$; (simulations M11, M12, M21 and M22); (b) Broad directional spreading $\sigma_\theta=30°$; (simulations M31, M32, M41 and M42).

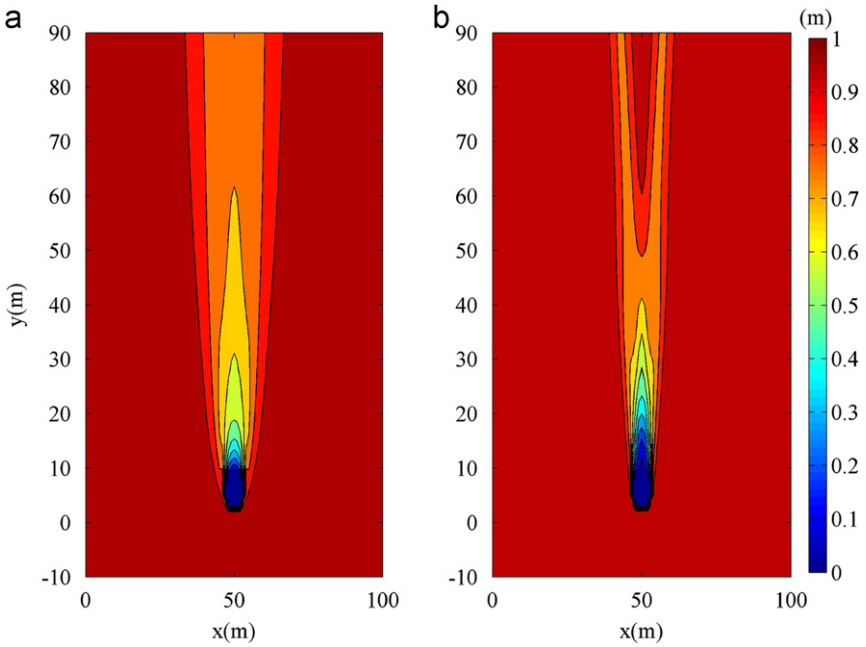

Fig. 5. Computed SWAN stationary H_s (m) map with diffraction (a), and without diffraction (b), for the JONSWAP spectrum with narrow directional spreading (simulations M11 and M21 in Table 2).

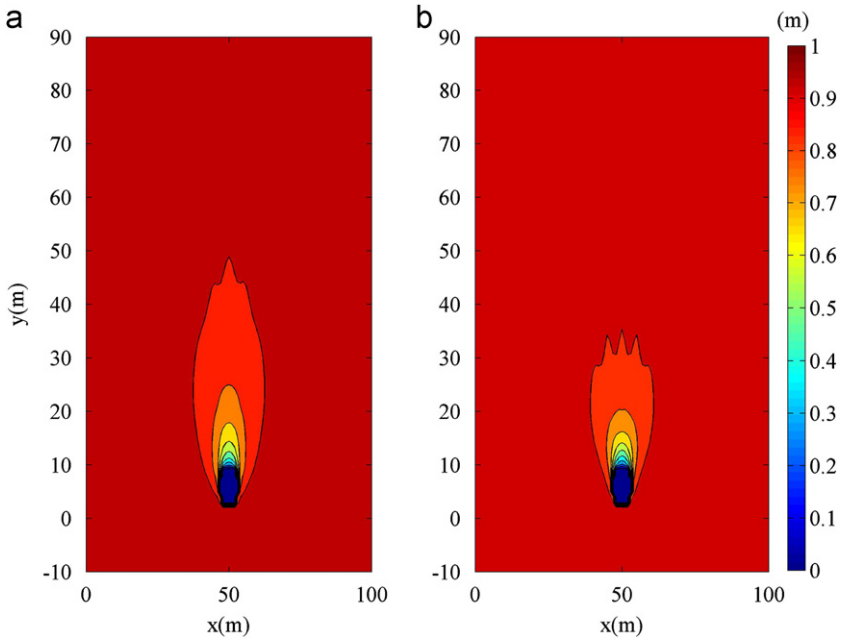

Fig. 6. Computed SWAN stationary H_s (m) map with diffraction (a), and without diffraction (b), for the JONSWAP spectrum with broad directional spreading (simulations M31 and M41 in Table 2).

existence of harmonic components following the contour of the monopile is more likely than in the narrow directional spreading case. Also, there is a slight increase in H_s in the down wave position. The reason for this is not completely clear, but it seems that the higher directional spreading contains some harmonic components traveling opposite to the main propagation direction just behind the monopile. That the case with reflection has slightly larger H_s seems to confirm that wave energy is being reflected back at the down wave position.

The significant wave height H_s maps are depicted in Fig. 5 (narrow directional distribution) and Fig. 6 (broad directional distribution), for the simulations without reflection. In the figures, panel (a) shows the results with diffraction turned on and panel (b) the results without diffraction. From the performed stationary simulations it can be seen that with narrow directional spreading the shadow zone behind the cylinder reaches the boundary of the simulation domain both with and without diffraction (Fig. 5, panels (a) and (b), respectively) but is slightly wider when diffraction is considered in the calculations. From Fig. 6 it can be seen that for the broad directional spreading, the length of the shadow zone behind the monopile is substantially reduced with respect to the narrow directional spreading calculations (Fig. 5). In this case, however, it is visible that the length of the shadow zone is slightly larger when diffraction is used (Fig. 6, panel (a)).

The length of the sheltered zone is related to the directional spreading of the wave energy spectrum due to the fact that wave energy propagation into the sheltered zone will depend on the directional width of the spectrum. Since the mean wave propagation direction is parallel to the sheltered zone in the absence of refraction induced by current or depth variations and diffraction, the propagation of energy into the sheltered zone will depend on the propagation directions of the harmonic components of the wave spectrum. Large directional spreading means that more energy is propagating at an angle to the mean wave propagation direction and some of these harmonic components will transport wave energy into the sheltered zone.

In Fig. 7 the H_s (a) and the directional spreading curves (b) for the case with narrow directional spreading, accounting for and omitting diffraction are shown along the shadow zone behind the monopile. From Fig. 7(a) it can be seen that the H_s behind the monopile is higher with diffraction than without diffraction, up to a 25 m distance from the monopile. At this distance, the rate of growth of H_s with diffraction is reduced substantially. Without diffraction, this reduction occurs much further away from the monopile. The evolution of the directional spreading behind the monopile shows a large difference (18° maximum at the first grid points behind the monopile) due to diffraction immediately after the monopile that is attenuated with increasing distance toward the boundary of the computational domain.

These results show two effects of diffraction: the increase of directional spreading immediately behind the monopile means that diffraction is enhancing the wave energy transport across the shadow zone behind the monopile, justifying the higher H_s seen in Fig. 7(a) and also that further down the shadow zone, diffraction will smooth the variation in H_s along the shadow zone.

4.4. Discussion

The results of the modeling approach of irregular wave interaction with a vertical cylindrical monopile show that there are drawbacks in the use of a spectral wave model. The drawbacks can be attributed to three reasons. The first is that spectral wave models cannot handle coherent wave patterns such as standing waves that occur in the up wave region of the monopile. This causes an under-estimation of the significant wave height just in front of the monopile, even when the obstacle is defined to be reflective.

Secondly, the monopile was modeled with obstacle lines, a feature in the SWAN model that is primarily intended to model linear obstacles in the path of the wave propagation. Since the monopile is itself impermeable, the transmission coefficient was set to zero. This created a region, behind the monopile, of much lower H_s than the analytical results from linear diffraction theory for unidirectional irregular waves. This fact is indicative of the limits of describing diffraction adequately in phase-averaging models. Third, the coarse representation of the cylinder led to a rough profile of H_s especially when reflection was used in the simulations. Spectral wave models such as SWAN were primarily thought for coastal regions with significantly higher spatial length scales O(100–1000 m) than those of the problem that was treated in this study O(1–10 m). This caused difficulties related to stability of the numerical methods employed by the model, due to the very high spatial resolution involved (1 m), which is more typical of laboratory than full scale studies. It was found that for large values of T_p, the simulations did not converge, probably due to the small size of the time step required to maintain the stability of the simulations. Note that the Courant number ($c_g\Delta t/\Delta x$) of the simulations increases both with increasing resolution and T_p since the group velocity c_g increases.

5. The problem considering the whole wind farm

5.1. Data

The adopted wind field for the hindcast study was the 6 hourly ERA-Interim reanalysis (Simmons et al., 2007) from the ECMWF (European Centre for Weather Medium Range Forecast). The wind data was retrieved on a $0.25^\circ \times 0.25^\circ$ grid and the wave models interpolate this wind information to specify the wind velocity components at every grid point in the implemented model grids.

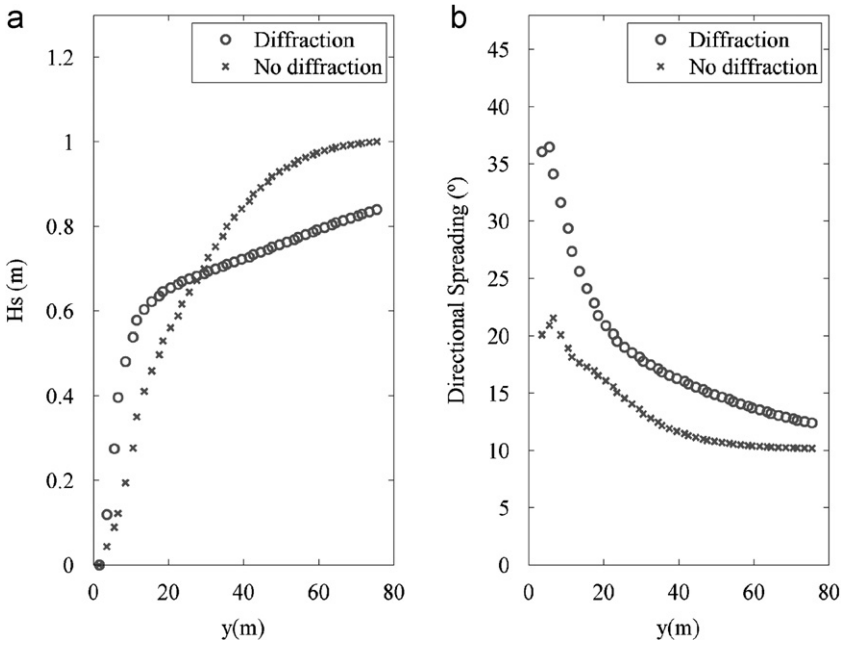

Fig. 7. Computed SWAN stationary (a) H_s (m) and (b) directional spreading (°) behind the windmill monopile for the JONSWAP spectrum with narrow directional spreading (simulations M11 and M21 in Table 2); (o-with diffraction; × -without diffraction).

The ERA-Interim wind field for 1st January 1992 at 06 UTC is represented in Fig. 8.

The hindcast study was performed from 1st December 1991 to 2nd January 1992 (32 days approximately 800 h) encompassing severe storm events that affected the Norwegian Sea region.

For the validation of the hindcast there was available the OCEANOR non directional buoy named Station Halten moored at 200 m depth located west outside of Mid-Norway. The coordinates of the buoy were 64.5°N and 7.7°E (magenta square in Fig. 8).

The WAM coarse and transitional nested bathymetry grids come from NOAA's GEODAS National Geophysical Data Centre (NGDC). The same data source was used for the first SWAN nested grid.

The bathymetry grid implemented for the HAVSUL-II area was taken from a very high resolution multibeam survey of the bottom, performed by the Norwegian company Sjøservice. The data has resolution of 1 m and is linearly interpolated to every 56 m for the geographical domain encompassing the northern part of HAVSUL-II, the region covers the area from: 62.65°N to 62.7°N and 6.0°E to 6.05°E (Fig. 9). This multibeam bathymetric survey was performed by Sjøservice specifically for the windmill installation project. In the HAVSUL-II region depths are in the range of 5–56 m. From the high resolution bathymetry (Fig. 9), two shallower zones can be distinguished with depths in the range of 5–15 m. The north region of the bathymetry grid is deeper than the southern side.

5.2. Validation of the wave hindcast results

One of the drawbacks of the hindcast study is the lack of measured wave data in the HAVSUL-II area with which to compare the model results, however, the results were validated for the WAM coarse grid (0.25°) at the Halten bank. The agreement of the measured H_s time series as compared with WAM coarse model is good for the simulation period (Fig. 10). Although the Halten bank location is far away from the western coast of Norway, it can be seen (at the end of the simulation period) that

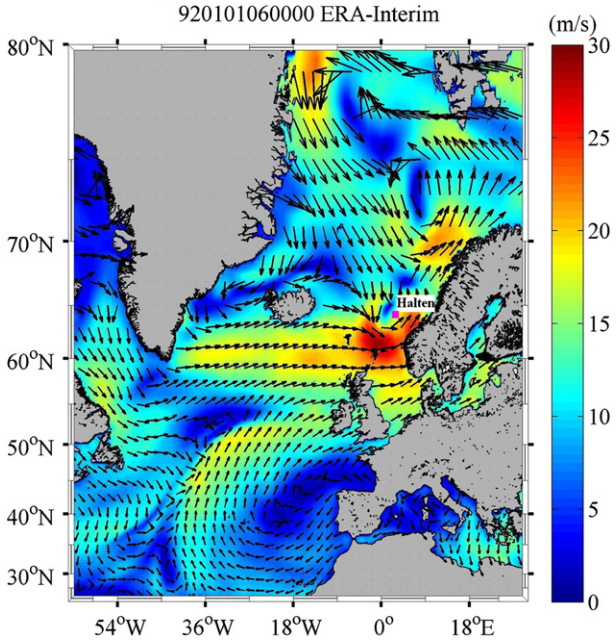

Fig. 8. ERA-Interim wind field dated the 1st January 1992 at 06 UTC and the location of the OCEANOR buoy named Halten (marked with magenta square). (For interpretation of the references to colour in this figure legend, the reader is referred to the web version of this article.)

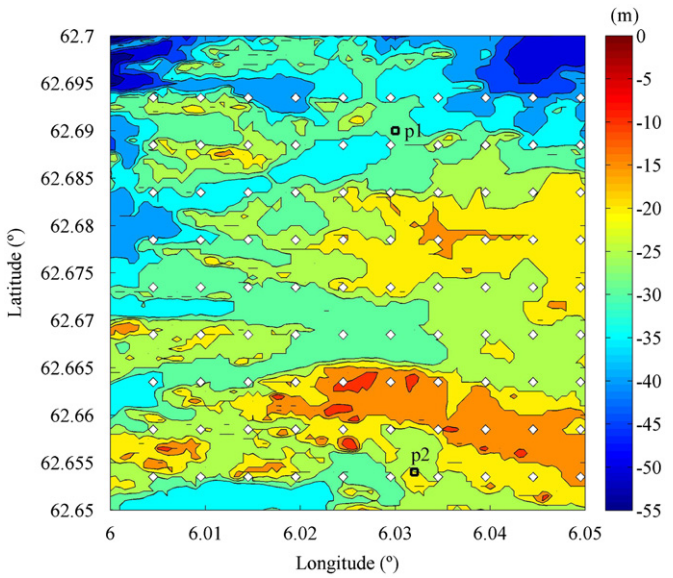

Fig. 9. The high resolution HAVSUL-II bathymetry, the 90 windmills and the wave models output locations marked with squares (location p1 at 32 m depth and coordinates: 6.03°E, 62.69°N; location p2 at 21 m depth and coordinates: 6.032°E 62.654°N).

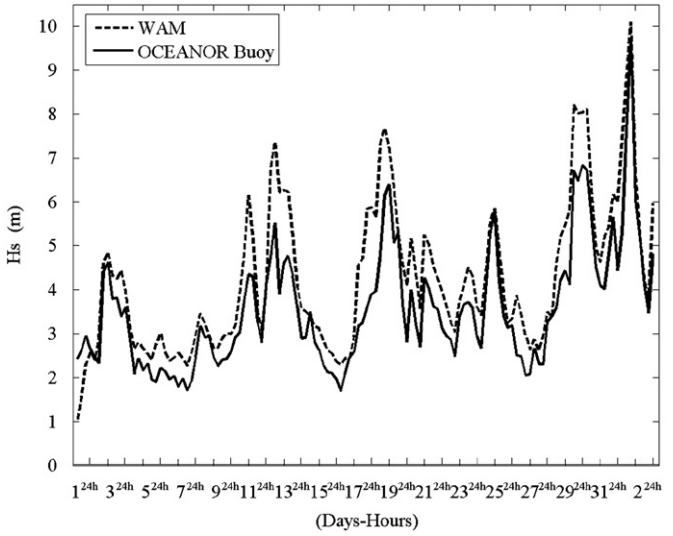

Fig. 10. Significant wave height H_s (m) time series comparison between the OCEANOR buoy data and the WAM coarse grid H_s results for the period 1st December 1991–2nd January 1992.

the maximum value of the H_s associated with the severe storm of 1st January 1992 (Aune and Harstveit, 1992) that caused several damages in the Møre og Romsdal region was almost 11 m.

The H_s map for this storm period (1st January 1992 at 06 UTC) is depicted in Fig. 11 from the WAM nested grid 1 (Table 3), from which it can be observed that H_s has values of around 11 m, associated with the storm, approaching from the SW to the HAVSUL-II study area.

Table 4 compiles the statistics for WAM simulations and buoy H_s time series at Halten bank. The mean absolute error is in order of 0.39 m; however, although the hindcasted values of the H_s correlate well with the measured data (see Fig. 10), WAM model overestimates the H_s at some of the recorded storms (negative biases of 0.6 m).

5.3. Setup of the hindcast study of the HAVSUL-II wind farm

The small size of the windmill monopile structure relative to the modeled HAVSUL-II offshore wind farm development site excludes the realistic representation of the whole set of windmills. Such a representation would require a spatial resolution similar in scale to the one used in the single windmill monopile study, which would result in a very high computational effort. For this reason each windmill monopile was represented as a dry point in the computational domain. The hindcast of the sea state for the high resolution HAVSUL-II domain in the both the presence and absence of the windmills was achieved by applying the SWAN model.

The hindcast study involved the application of the WAM and SWAN models with four nesting levels (Table 3). The WAM coarse grid was implemented covering the North Atlantic (25°N, 80°N, 30°E, 64°W) with a resolution of approximately 27.8 km (0.25°) in latitude and longitude. This was followed by the first transitional WAM nested grid (61°N, 65°N, 0°E, 7°E) for the region covering the offshore area of Møre og Romsdal, followed by the first SWAN coarse grid (61°N, 63°N, 5°E, 7°E) using the boundary conditions generated in the previous WAM grid. The final level of nesting was a SWAN grid encompassing the HAVSUL-II area where the installation of 90 windmills is planned (HAVSUL-II nested grid 2 in Table 3).

The 90 windmill monopiles were represented in the high resolution bathymetry grid by dry points separated by a distance of 560 m (ten grid spacings apart). The analyzed region, located in the north part of the HAVSUL-II project area had its own complexity and it was represented by a square box with the limits specified in Table 3 (HAVSUL-II nested grid 2). The spatial resolution in X and Y was 56 m (0.0005°) for a total number of 10201 (101×101) points (Table 3). At this spatial resolution the HAVSUL-II nested grid with the SWAN model required an integration time step of 60 s. Simulations with 30 windmill monopiles were also conducted in order to study the effect of the number of monopiles in the wave field and to avoid any influence from the boundaries, since in the 90 windmills setup some monopiles were placed very close to the East boundary.

The WAM and SWAN models numerically integrated the wave energy transport Eq. (1) for 24 directions and 25 frequency bands.

The lowest resolved frequency was 0.0418 Hz. The initial condition for the WAM model was a JONSWAP spectrum, with the following parameters: Phillip's parameter, 0.018; peak frequency, 0.2 Hz; overshoot factor, 3; left width, 0.07; right width, 0.09; averaged wave direction, 0.0 and fetch, 30 km.

In the SWAN hindcast simulations the default propagation scheme was used. For the nonstationary simulations the default scheme is the first order upwind scheme also known as the first order backward space, backward time (BSBT). This scheme is unconditionally stable, although it is prone to numerical diffusion effects (Rogers et al., 2002).

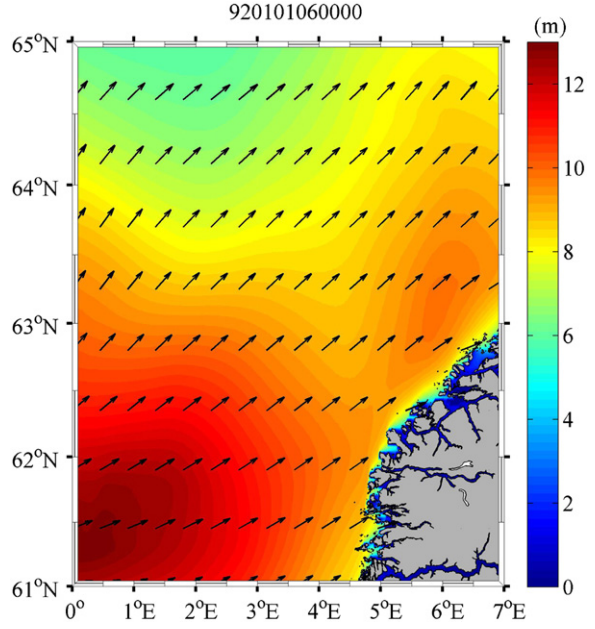

Fig. 11. WAM H_s (m) map and mean wave propagation direction (arrows) during the storm of 1st January 1992 at 06 UTC.

5.4. Results and discussions

To assess the performance of SWAN model, without/with windmills and diffraction process activated, a comparison of the H_s maps distribution is depicted in Fig. 12 for 5th December 1991 at 12 UTC. A clear change of the mean wave direction can be observed in the southeast part of the grid (shallower waters) with the 90 windmills (right panel). This effect was less pronounced with 30 windmills and was not observed without windmills. A sensitivity analysis using a different integration time step of 10 s was performed to verify a possible time step effect. For this analysis the same processes indicated in Table 1 were kept but

Table 4
Statistical parameters between the Halten buoy data and WAM simulations results for the H_s (m) for the period 1st December 1991 up to 2nd of January 1992 (STD-standard deviation; RMSE-root mean square error of the difference; SI—scatter index; MAE-mean absolute error). Mean buoy H_s value=3.55 m, Mean WAM Hs value=4.2 m.

Parameters	Halten
STD	0.6
Bias	−0.6
RMSE	0.91
SI	38.6
Slope	0.85
MAE	0.39

Table 3
Numerical parameters for the WAM and SWAN hindcasts.

Parameters	WAM (coarse grid)	WAM (nested grid 1)	SWAN (nested grid 1)	SWAN (HAVSUL-II nested grid 2)
Integration and source function time steps (s)	160	50	180	60
Spatial resolution	0.25° (27864 m)	0.025° (2786.4 m)	0.008° (892 m)	0.0005° (56 m)
Number of points (x,y)	(377,221)	(281,161)	(251,251)	(101,101)
Propagation	Spherical	Spherical	Spherical	Spherical
Type of model	Deep water	Deep water	Shallow water	Shallow water
Latitudes, (°N)	25; 80	61; 65	61; 63	62.65; 62.7
Longitudes, (°E)	30	0; 7	5; 7	6.0; 6.05
Longitudes, (°W)	64	–	–	–

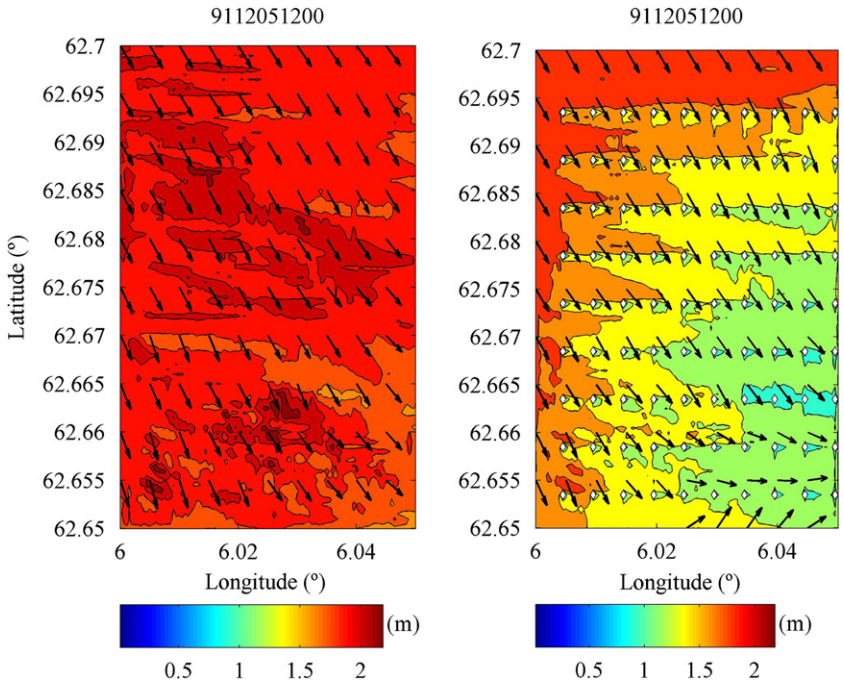

Fig. 12. SWAN H_s (m) maps for 5th December 1991 at 12 UTC (left-without windmills; right-with 90 windmills).

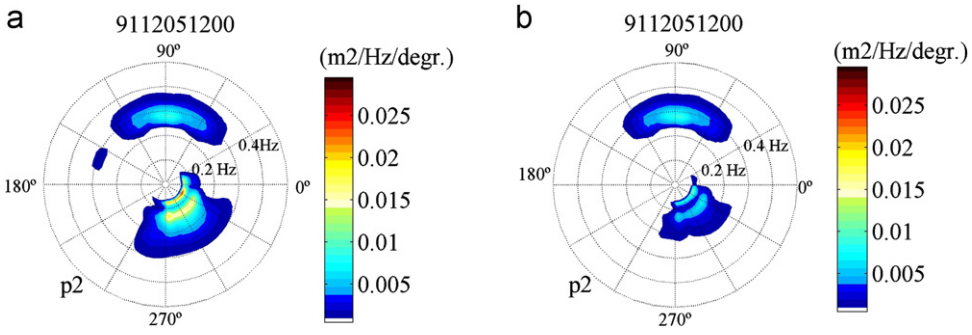

Fig. 13. SWAN computed bidimensional wave spectra for 5th December 1991 at 12 UTC at p2 (a) without windmills; (b) with 90 windmills.

the simulations were only performed for the case of 90 windmills. The results from this sensitivity analysis with different time steps (1 min and 10 s) did not present noticeable differences looking at the spatial distribution of the H_s and the mean wave propagation direction. However, some small differences of the order of 5 cm were observed locally at locations p1 and p2 (not shown). All the numerical results presented for this study were made with a time step of 1 min. The effect of the turning of mean wave propagation direction to the NE in the South East part of the grid was observed under wind speeds lower than 7 m/s (from the NW for 5th December 1991 at 12 UTC). The referred effect could probably be associated with the representation of the windmill monopiles as dry points (land points absorbing all incoming wave energy). The effect of the dry point is similar to that of the point inside an obstacle, i.e., it will lower the value of wave energy calculated in the neighboring wet points during the propagation of wave energy by upwind procedures. This effect can be seen in Fig. 12 as shadow zones on the down wave region around some of the dry points representing the windmills.

To gain a better insight on the windmills influence on the reduction of the wave energy the SWAN bidimensional wave spectra at location p2 (see Fig. 9) are represented in Fig. 13 for 5th December 1991 at 12 UTC. From the spectra it can be inferred that a second consequence of accounting the 90 windmills is the modification of the shape of the spectrum (Fig. 13b). At p2 wave spectra with a complex shape (three-peaked) were observed. When the windmills are present, the reduction in spectral energy is clearly seen (Fig. 13(b)). This reduction occurs in the spectral energy that is contained in the upwind sector (sector from where the waves are propagating) because the upwind monopiles have decreased the energy of the incoming waves. Due to this reduction of spectral energy in this sector, the three spectral peaks have similar values of energy and this causes the mean direction of wave propagation to rotate northwards. The respective source function terms, their sum S_{tot} and the one dimensional spectrum $E(f)$ are represented in Fig. 14. Bottom friction dissipation S_{bf} and nonlinear wave–wave interactions (S_{nl4}) are the more noticeable processes. S_{nl4}, which are important in the spectral balance play the role of the redistribution of the excess high frequency part wave energy towards the low frequencies. The other physical processes remain weak (S_{in}, S_{nl3} and S_{wcap}). Performing the simulation with 90 windmills the physical processes seem to be weaker than without windmills (top). In particular, S_{bf} decreases due to the decrease in wave energy when the windmills are included in the simulations.

Overall one of the consequences of the windmills is the blocking of wave energy propagating from the Western side of the grid (Fig. 12, right panel). The monopiles act as obstacles

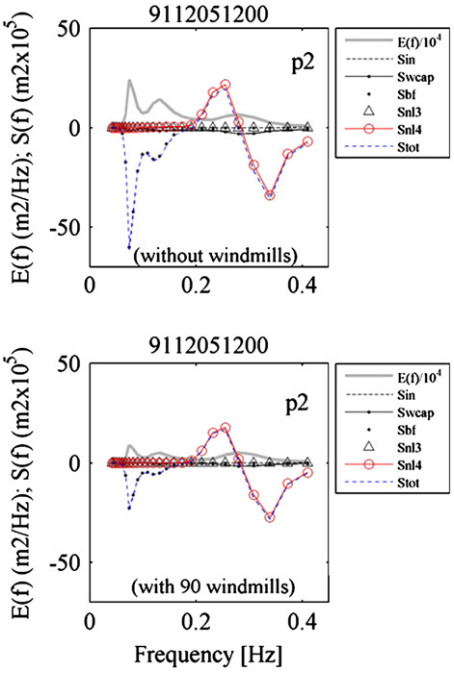

Fig. 14. SWAN computed source functions terms (S_{in}—wind input; S_{wcap}—white capping wave energy dissipation), S_{bf}—bottom friction dissipation; S_{nl3} and S_{nl4}—nonlinear triad and quadruplets, sum of the all source functions (S_{tot}) and the variance spectrum ($E(f)$) for 5th December 1991 at 12 UTC at p2 (top—without windmills; bottom—with 90 windmills).

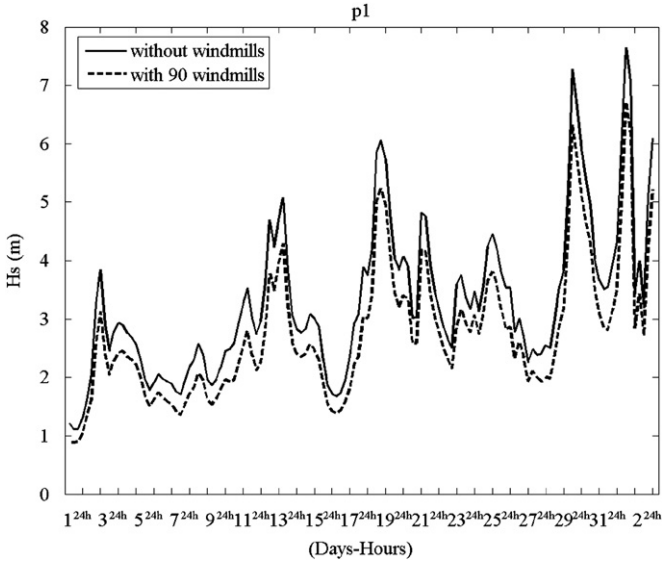

Fig. 15. Computed SWAN H_s time series at location p1 for 1st December, 1991 up to 2nd January 1992 with/without windmills.

blocking the propagation of wave energy and induce a change in the wave propagation direction. Locally behind every monopile a shadow can be seen which, on some locations, can reach the neighboring monopile. This is the effect of their modeling as dry points, as discussed above.

As a consequence the 90 windmills seem to act globally as an obstacle affecting the wave field. The shoaling phenomenon is also evident associated with reduced depths (5–8 m) in the shallower zone where the average depth is about 15 m (see Fig. 9). Accounting for the windmills in the numerical domain, the shoaling appeared smoothed and modified by these obstacles (Fig. 12, right).

To assess the impact of 90 windmills on the significant wave height a comparison of SWAN forecasted H_s time series both with and without windmills is given in Fig. 15 at location P1 inside the farm (see Fig. 9). In general, it can be seen that with the 90 windmills the H_s decreases. The activated processes for these SWAN simulations are represented in Table 1.

To avoid any influence from the boundaries, additionally SWAN simulations accounting for the all processes and with diffraction activated (Table 1) were performed with only 30 monopiles in the center of the HAVSUL-II nested grid 2 domain (Fig. 16, right panel). From the H_s maps (left and right panels) the larger number of windmill monopiles, induce a larger reduction of the H_s (Fig. 16, left panel), whereas the H_s with fewer obstacles is higher (Fig. 16, right) due to the reduction of the windmill monopile's global blocking effect on the wave energy. To allow the analysis of the effect of the number of windmills on the wave energy the bidimensional wave spectra at p1 for the peak of the storm of 1st January 1991 at 06 UTC are given in Fig. 17. It can be seen that with 90 windmills (Fig. 17a) the spectrum shape is slightly narrower than with 30 windmills. However, both spectra exhibit similar wave energy. It is necessary to point out that for the case of 90 windmills p1 is inside the farm and for the case of 30 windmills this location is outside the farm.

Fig. 18 displays all the physical processes at location p1 (see Fig. 9) with 90 windmills (top) and with 30 windmills (bottom). From the spectral shapes of the source functions can be seen that triad interactions (S_{nl3}) are the weakest of all the processes. The bottom friction (S_{bf}) dissipation was observed the most intense process in both cases (with 30 and 90 windmills). However, the whitecapping dissipation was less intensive in presence of the 90 windmills (top panel). The wind input source term S_{in} contribution was highly noticeable in accordance with the wind speed that for this date was about 27 m/s in the region of HAVSUL-II with a main direction from the SW (Fig. 8). Note that with this higher value of wind velocity the shadow area behind the monopiles is less noticeable. This is due to a higher input of energy by the wind source term, which partially compensates for the dry point effect.

6. Nonstationary single monopile

6.1. Simulations setup

For completeness nonstationary simple propagation simulations (in the 100 m × 100 m domain) were performed with the SWAN wave model with boundary conditions (wave spectra) obtained from the HAVSUL-II SWAN simulations (HAVSUL-II nested grid 2 in Table 3) at location p1 (Fig. 9). These computations correspond to three days, from the 31st December of 1991 at 00 UTC to 2nd January 1992 at 18 UTC to investigate under realistic waves conditions the transformation of the wave field behind a single windmill monopile. In addition, diffraction process was activated for these simulations.

The calculation domain is the same as in the previous stationary simulations with the monopile. The computational boundaries orientation correspond to the larger simulation domain, i.e., waves with mean propagation direction due East enter the calculation domain from the western border. The monopile was relocated inside the domain to a location 14.4 m east from the western boundary, halfway between the South and North boundaries. The cylinder relocation was decided to better assess the cylindrical monopile impact on the wave field behind it; for the simulation period chosen (winter 1991–1992) the mean wave propagation direction was mainly from the West sector. The depth of the domain was uniform and equal to 30 m.

Since the computational domain with the cylindrical monopile is small compared to the HAVSUL-II simulation domain, a uniform

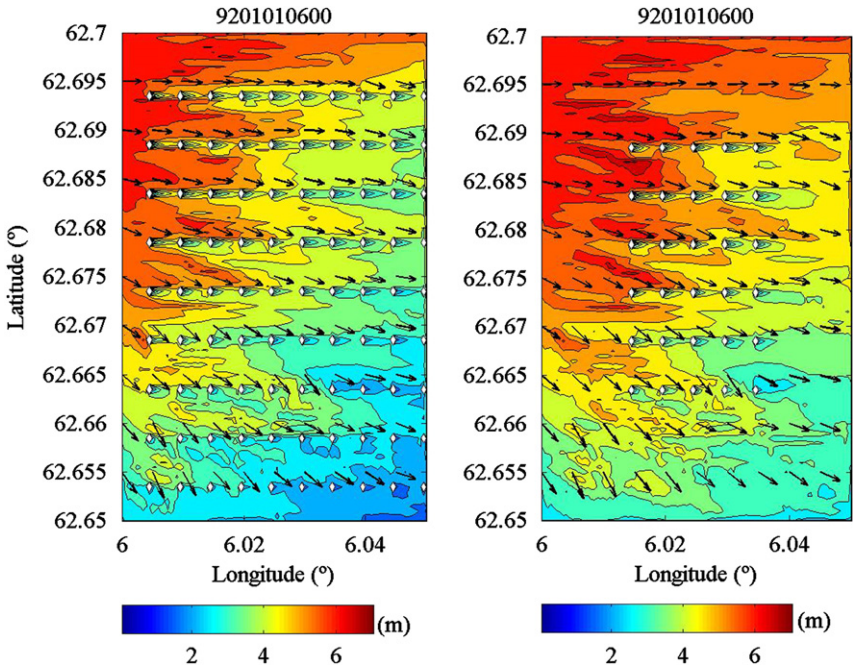

Fig. 16. Computed SWAN H_s (m) maps, accounting the 90 (left) and 30 (right) windmills for 1st January 1992 at 06 UTC.

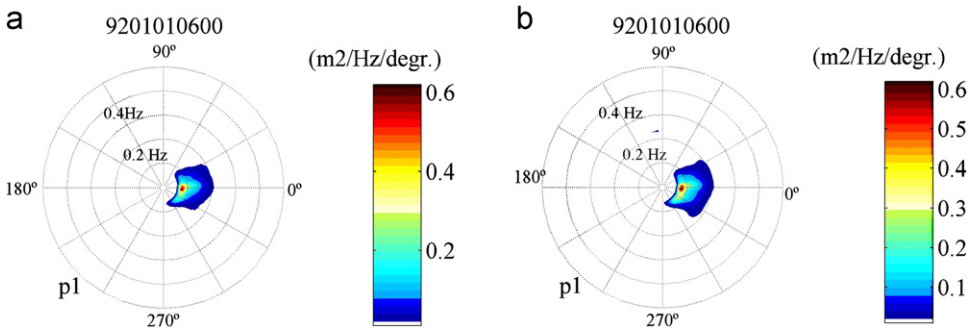

Fig. 17. SWAN computed bidimensional wave spectra for 1st January 1992 at 06 UTC at p1 (a) with 90 windmills; (b) with 30 windmills.

wave spectrum in the four boundaries of the domain was applied. The time step of the simulations was set at 60 min with the boundary wave spectrum updated every 6 h. The propagation scheme used was the BSBT scheme. Note that this scheme is unconditionally stable so higher time steps can used.

6.2. Results and discussion

From these simulations two dates were selected to analyze the transformation of the wave field behind the monopile. The incoming wave spectra propagates mainly from the NW (1st January 1992 at 18 UTC) and from the West (2nd January 1992 at 18 UTC) as seen in Fig. 19 (top and bottom panels, respectively). The bidimensional boundary spectra used as the incoming wave energy for these were taken from location p1 (see Fig. 9) for the case without windmills are shown in Fig. 20. The top spectrum represents higher wave energy level than the bottom spectrum.

For the 1st January the shadow zone created by the monopile in the down wave direction is not symmetric in both cases (with and without diffraction). We believe the reason for this is the coarse representation of the monopile. In fact, the distribution of the grid points inside the obstacle lines is symmetric with respect to the wave (mean) propagation direction only if the waves are entering the domain from the West as in the case of 2nd January (Fig. 19, bottom panels). This is a drawback of using a coarse resolution to represent the monopile.

The effect of diffraction is clearly seen in the H_s map of the 1st January (Fig. 19, top panels). The use of diffraction seems to create two shadow zones approximately aligned with the reference directions (S–N and W–E). The fact that this effect is missing in the map of 2nd January with diffraction (Fig. 19, bottom left panel) indicates that this could be caused by the lack of symmetry in the monopile representation, discussed above. This, together with the effect of diffraction increasing the length of the shadow zone (see Section 4.3) could explain the increased length of the shadow zone in the N–S direction. On the other hand, for the later date (Fig. 19, bottom panels) the monopile representation is symmetric and the shadow zones are practically similar.

The reduced length of the shadow zone can be related to the broad directional spreading of the incoming wave spectra in the two dates – approximately 35° for both dates – shown in Fig. 19. This relationship was found to exist also for the stationary monopile simulations (Section 4) were it was shown that a higher directional spreading led to a shorter shadow zone behind the monopile.

To assess how the monopile effect changes with distance three day averaged H_s (m) curves are analyzed along a path behind the cylinder in the West–East direction, as represented in Fig. 21. These averaged H_s curves show how the effect of the cylinder in reducing the H_s is attenuated with increasing distance from the

monopile. In average the H_s decreases 50 cm at 20 m behind the monopile. The impact of the windmill monopile is noticeable up to the eastern domain boundary although losing significance after the first 20 m behind the monopile.

The three days (31st December 1991, 1st and 2nd January 1992) SWAN one dimensional spectra averaged are displayed in Fig. 22. These spectra are obtained at four locations: LOC1 is located in front of the monopile ($x=5$ m; $y=40$ m); LOC2, LOC3 and LOC4 are behind the monopile at 11, 36 and 80.6 m from the cylinder, respectively, with coordinates ($x=25$ m; 50 m; 95 m and $y=40$ m) in the 100 m × 100 m nested domain; Fig. 22 shows the reduction that the wave energy computed at the peak of the spectrum may experience immediately behind the monopole reaching 37%. This reduction vanishes with distance, and at LOC3 decreases to 15.7%. Already near the East boundary the swell energy reduces on average a 4.24% as can be seen in Fig. 22.

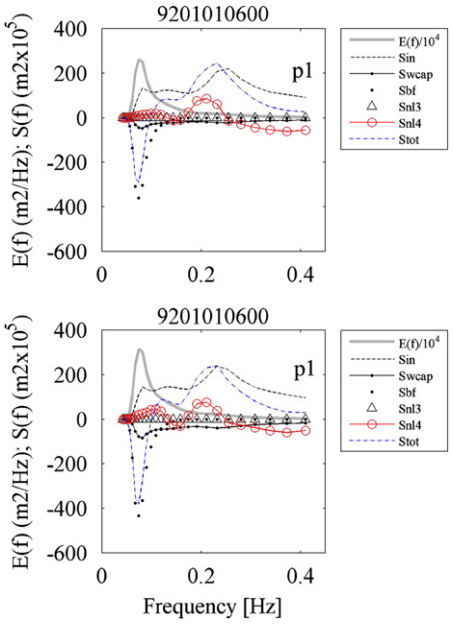

Fig. 18. SWAN computed source functions terms (S_{in}—wind input; S_{wcap}—white-capping wave energy dissipation), S_{bf}—bottom friction dissipation; S_{nl3} and S_{nl4}—nonlinear triad and quadruplets, sum of the all source functions (S_{tot}) and the variance spectrum ($E(f)$) for 1st January 1992 at 06 UTC at p1 (top—with 90 windmills; bottom—with 30 windmills).

7. Concluding remarks

A numerical study of irregular waves in the HAVSUL-II offshore wind farm in the Norwegian continental shelf was conducted

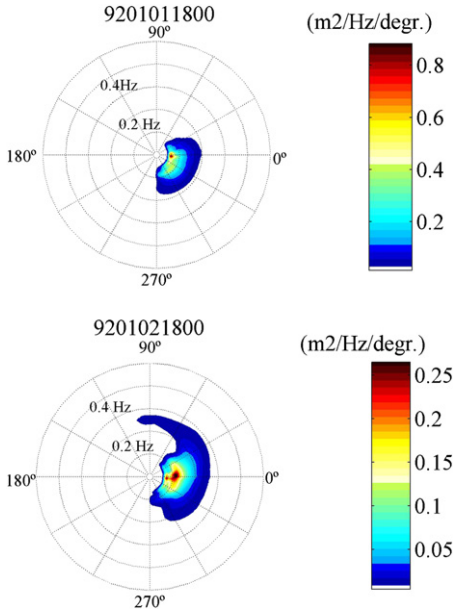

Fig. 20. The bidimensional boundary spectra used for the nonstationary single monopile simulations given at p1 from the case without windmills for the dates January 1st at 18 UTC (top) and January 2nd at 18 UTC (bottom).

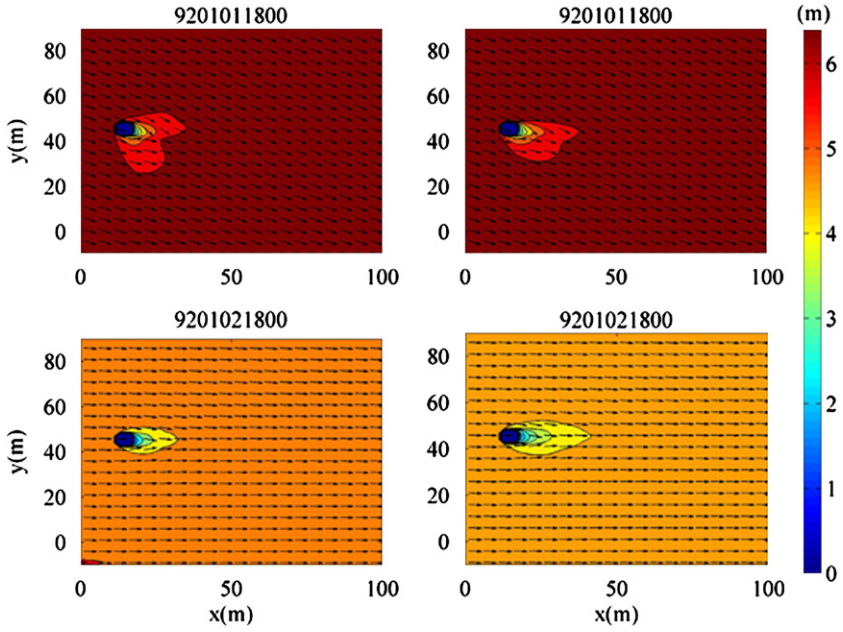

Fig. 19. Computed SWAN nonstationary H_s (m) map and mean wave propagation direction (arrows) with diffraction (left panels) and without diffraction (right panels) during two selected dates: 1st January 1992 and 2nd January 1992 at 18U TC.

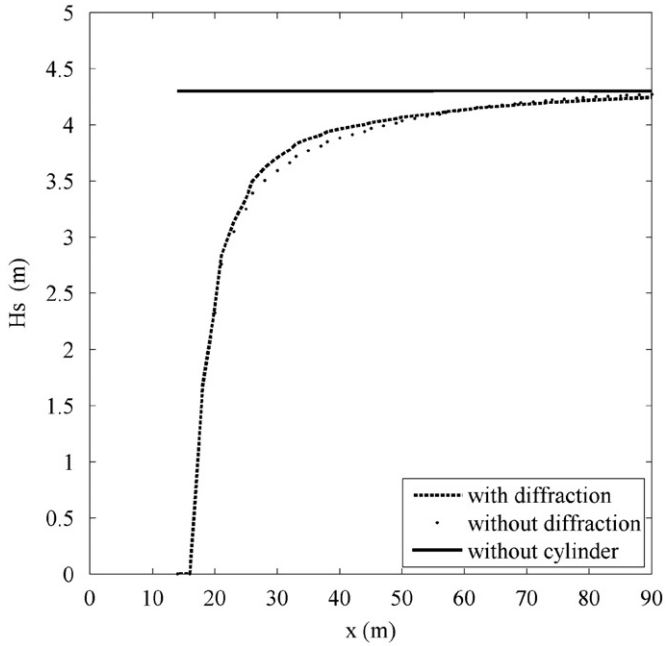

Fig. 21. Computed SWAN nonstationary H_s (m) averaged over three days (31st December 1991, 1st and 2nd January 1992) behind the windmill monopile with diffraction (dashed line), without diffraction (dot line), without the monopile (solid line).

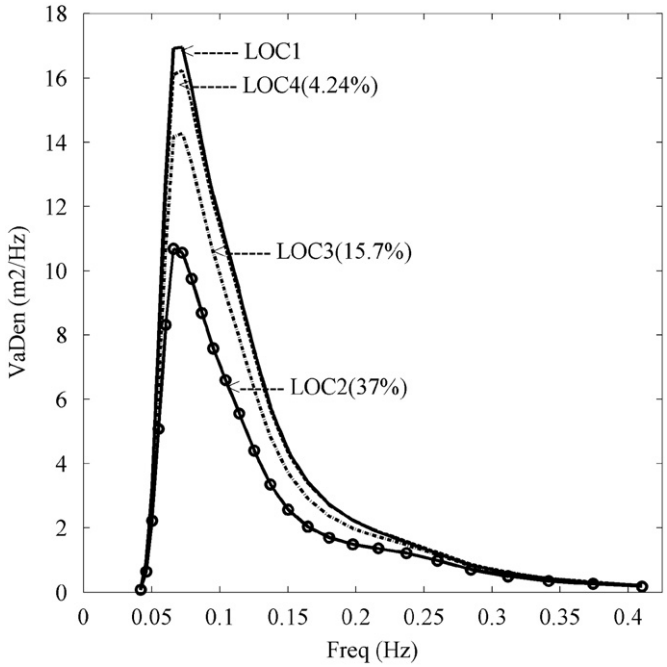

Fig. 22. Computed SWAN one dimensional spectra averaged over three days (31st December 1991, 1st and 2nd January 1992) at locations LOC1, LOC2, LOC3, LOC4; LOC1-located in front of the monopile (x=5 m; y=40 m); LOC2, LOC3 and LOC4 located behind the monopile with coordinates (x=25 m; 50 m; 95 m and y=40 m).

using spectral wave models. The offshore wind farm is composed of 90 wind turbines, each 95 m high and supported by cylindrical monopiles with a diameter of 6 m and separated from each other 540 m. The wave climate in the area is mainly the North Atlantic long period swell with narrowly peaked spectra with considerable energy at periods higher than 15 s.

The study was divided in two parts: the study of the effect of a single windmill monopile in the incoming waves using the SWAN spectral wave model in stationary mode and a hindcast study of the wave field in the offshore wind farm area with and without the windmills using two spectral wave models (WAM and SWAN). The effect of a single windmill monopile on incident waves with realistic spectra from the hindcast was also performed.

In the stationary study the monopile was represented as an obstacle in the computational domain. The obstacle representation influenced the results due to the treatment of the wave energy propagation in its vicinity, creating a shadow zone behind the monopile. The accuracy of the monopile representation had a great impact on the computed H_s around the monopile. The phase-decoupled diffraction model available in SWAN was used to model diffraction effects of the interaction of the irregular incoming waves with the monopile. The effects of diffraction were a smoothing of the H_s distribution both around the monopile and on the shadow zone behind it, being more pronounced in the latter. When reflection was used, diffraction acted to smooth the rough profile of H_s in the up wave region of the monopile, caused by the coarse representation of its cylindrical shape. Globally, the effects of diffraction were not very pronounced when compared to reflection that changed the H_s distribution in front of the monopile in an appreciable manner.

The directional spreading of the incoming irregular waves proved to have a great influence in the results. It was shown that higher directional spreading caused a reduction in the length of the shadow zone and also a smoother distribution of H_s in the up wave region of the monopile. In fact, the increase of the directional spread of the incoming waves resulted in an H_s distribution closer in shape to the one obtained analytically. This is because the analytical theory predicts a reflected wave all around the monopile perimeter, which is best approximated by a broad directional spectrum that could contain harmonic components propagating toward the monopile not only in the up wave region. This is, however, an incidental similarity, since linear theory predicts this reflected wave for a purely monochromatic wave.

The hindcast study was conducted by nesting successively finer grids from a 0.25° coarse grid up to a high-resolution 56 m grid covering 26.2 km^2 of the HAVSUL-II offshore windmill farm for a specific winter period. The hindcast results were validated with buoy measurements for the coarser grid. Due to the small size of the windmill monopiles they were represented as dry points in the high-resolution hindcast of the HAVSUL-II area.

The comparison of the significant wave height fields with and without the offshore wind farm present shows that the group of windmill monopiles may contribute to the reduction of the swell energy inside the offshore wind farm area. From the hindcast simulations it seems that once the waves enter into the offshore wind farm they experience modifications due to the presence of the windmill monopiles, which cause a blocking of the wave energy propagation, resulting in an altered distribution of the wave field.

The study of the single monopile with realistic spectra showed that it may reduce the typical North Atlantic continental shelf swell energy in 4.24% (estimated in average at the spectral peak and taken at 80.6 m from the cylinder in the sheltered zone). For this study, diffraction effects were noticed mainly when the incoming wave direction deviated from the S–N or W–E directions, although this was due principally to the coarse representation of the monopile. Other studies looking at diffraction by applying the SWAN model have shown that diffraction is very sensitive to the spatial resolution inducing enhancements in the significant wave height (Rusu et al., 2008). In the case of the present whole wind farm simulations, the diffraction effect does not appear clear due to the 56 m spatial resolution adopted for the set of 90 windmills.

The areas where offshore wind farms are located are normally exposed to severe wind and wave conditions and this is also the

case for the HAVSUL-II area studied in this paper. The reduction of the significant wave height inside the HAVSUL-II offshore wind farm was shown in our study. These reductions were mainly due to the representation of the monopiles as obstacles (stationary study) and dry points (hindcast study), which acted in a way that can best be described as absorbing the incoming wave energy. In reality, wave energy will be dissipated through drag and inertia effects that at the moment were not included in the present work. In addition, other local effects such as vortex shedding or wind wake from the windmill monopile could also contribute to modifications of the significant wave height. These subjects deserve to be investigated in future studies.

Acknowledgments

The authors would like to thank the Norwegian Sjøservice Company for providing the bathymetry data of the area of HAVSUL-II. Many thanks to Dr. Øyvind Sætra from the Meteorological Office of Oslo, who retrieved the ERA-Interim wind field. Also thanks to Dr. Stephen Barstow, who supplied the OCEANOR buoy data. We are grateful to Prof. Lucy Wyatt from Sheffield University for her comments to the first version of the manuscript. We would also like to thank the anonymous reviewers, who helped us to improve the manuscript with their valuable comments and suggestions. Sonia Ponce de León is presently supported by the Ministry of Science and Innovation of Spain (MICINN-JDJ). J. H. Bettencourt is currently supported by the portuguese Foundation for Science and Technology (FCT).

References

Alari, V., Raudsepp, U. Simulation of wave damping near coast due to offshore wind farms. Journal of Coastal Research, in press. doi:10.2112/JCOASTRES-D-10-00054.1.

Aune, B., Harstveit, K., 1992. The Storm of January 1st 1992. Rapport NR. 23/92. DNMI KLIMA Det Norske Meteorologiske Institute.

Berkhoff, J.C.W., 1972. Computation of combined refraction-diffraction. In: Proceedings of the Thirteenth International Conference on Coastal Engineering, ASCE, pp. 471–490.

Booij, N., Ris, R.C., Holthuijsen, L.H., 1999. A third generation wave model for coastal regions. Part 1: model description and validation. Journal of Geophysical Research 104 (C4), 7649–7666.

Beels, C., Troch, P., De Backer, G., Vantorre, M., De Rouck, J., 2010. Numerical implementation and sensitivity analysis of a wave energy converter in a time-dependent mild-slope equation model. Journal of Coastal Engineering 57, 471–492.

Cooper, B., Beiboer, F., 2002. Potential Effects of Offshore Wind Developments on Coastal Processes. ETSU W/35/00596/00/REP, URN 02/1336, Technical Report 70 pp.

Dean, R.G., Dalrymple, R.A., 1991. Water wave mechanics for engineers and scientists. In: Liu, Phillip L.-F. (Ed.), Advanced Series on Ocean Engineering, vol. 2. World Scientific Publishing, Singapore, pp. 351.

Eatock Taylor, R., 2007. On modelling the diffraction of water waves. Ship Technology Research 54 (28th Georg Weinblum Memorial Lecture).

Eldeberky, Y., 1996. Nonlinear Transformation of Wave Spectra in the Nearshore Zone. Ph.D. thesis, Delft University of Technology, Department of Civil Engineering, The Netherlands.

Gjevik, B., Krogstad, H.E., Lygre, A., Rygg, O., 1988. Long period swell events on the Norwegian Shelf. Journal of Physical Oceanography 18, 724–737.

Günther, H., Hasselmann, S., Janssen, P.A.E.M., 1992. The WAM model Cycle 4 (revised version), Deutsch. Klim. Rechenzentrum, Techn. Rep. No. 4, Hamburg, Germany.

Hasselmann, S., Hasselmann, K., Allender, J.H., Barnett, T.P., 1985. Computations and parameterizations of the nonlinear energy transfer in a gravity wave spectrum. Part II: parameterizations of the nonlinear transfer for application in wave models. Journal of Physical Oceanography 15 (11), 1378–1391.

Havelock, T.H., 1940. The pressure of water waves upon a fixed obstacle. Proceedings of the Royal Society of London A 175, 409–421.

Holthuijsen, L.H., Herman, A., Booij, N., 2003. Phase-decoupled refraction diffraction for spectral wave models. Journal of Coastal Engineering 49, 291–305.

Ilic, S., Van der Westhuysen, A.J., Roelvink, J.A., Chadwick, A.J., 2007. Multidirectional wave transformation around detached breakwaters. Journal of Coastal Engineering 54, 775–789.

Janssen, P.A.E.M., 1989. Wave-induced stress and the drag of air flow over sea waves. Journal of Physical Oceanography 19, 745–754.

Janssen, P.A.E.M., 1991. Quasi-Linear theory of wind wave generation applied to wave forecasting. Journal of Physical Oceanography 21, 1631–1642.

Kjerstad, N., 2006. Simulation and assessment of navigation close to offshore wind farms. In: Proceedings of the ISOPE-2006, International Society of Offshore and Polar Engineer, San Francisco, CA.

Komen, G.J., Hasselmann, S., Hasselmann, K., 1984. On the existence of a fully developed wind-sea spectrum. Journal of Physical Oceanography 14, 1271–1285.

Kriebel, D.L., 1990. Nonlinear wave interaction with a vertical circular cylinder. Part I: diffraction theory. Journal of Ocean Engineering 17 (4), 345–377.

Linton, C.M., Evans, D.V., 1990. The interaction of waves with arrays of vertical circular cylinders. Journal of Fluid Mechanics 215, 549–569.

MacCamy, R.C., Fuchs, R.A., 1954. Wave Forces on Piles: A Diffraction Theory. US Army Corps of Engineering, Beach Erosion Board, Washington, DC (Tech. Mem. 69).

Maniar, H.D., Newman, J.N., 1997. Wave diffraction by a long array of cylinders. Journal of Fluid Mechanics 339, 309–330.

Mei, C.C., 1992. The applied dynamics of ocean surface waves. In: Liu, Phillip L.-F. (Ed.), Advanced Series on Ocean Engineering, vol. 1. World Scientific Publishing, Singapore, pp. 735.

Rao, P.S.V., Raman, H., 1988. Wave elevation on large circular cylinders excited by wind-generated random waves. Transactions of the ASME 110, 48.

Reistad, M., Magnusson, A.K., Haver, S., Gudmestad, O.T., Kvamme, D., 2005. How severe wave conditions are possible on the Norwegian Continental Shelf? Journal of Marine Structures 18, 428–450.

Ris, R.C., 1997. Spectral modeling of wind waves in coastal areas. Communications on Hydraulic and Geotechnical Engineering, Delft University of Technology, 157 p.

Rogers, W.E., Kaihatu, J.M., Petit, H.A.H., Booij, Holthuijsen, L.H., 2002. Diffusion reduction in an arbitrary scale third generation wind wave model. Journal of Ocean Engineering 29, 1357–1390.

Rusu, E., Pilar, P., Guedes Soares, C., 2008. Evaluation of the wave conditions in Madeira Archipelago with spectral models. Journal of Ocean Engineering 35, 1357–1371.

Simmons, A., Uppala, S., Dee, D., Kobayashi, S., 2007. ERA-Interim: New ECMWF Reanalysis Products from 1989 Onwards. ECMWF Newsletter No. 110, 25–34.

SWAN Group, 2010. Swan Scientific and Technical Documentation. Department of Civil Engineering and Geosciences, Delft University of Technology, Delft, The Netherlands 119 p.

Walker, D.A.G., Eatock Taylor, R., 2005. Wave diffraction from linear arrays of cylinders. Journal of Ocean Engineering 32, 2053–2078.

Young, I.R., 1999. Wind generated ocean waves. In: Bhattacharyya, R., McCormick, M.E. (Eds.), Ocean Engineering Series. Elsevier, Amsterdam, pp. 288.

Zhu, S., 1993. Diffraction o short-crested waves around a circular cylinder. Journal of Ocean Engineering 20, 389–407.